Efficient oxygen reduction to H2O2 in highly porous manganese and nitrogen co-doped carbon nanorods enabling electro-degradation of bulk organics

Biemolt, J.; van der Veen, K.; Geels, N.J.; Rothenberg, G.; Yan, N.

DOI
10.1016/j.carbon.2019.09.034

Publication date
2019

Document Version
Final published version

Published in
Carbon

Carbon 155 (2019) 643–649

Contents lists available at ScienceDirect

Carbon

journal homepage: www.elsevier.com/locate/carbon

Efficient oxygen reduction to H_2O_2 in highly porous manganese and nitrogen co-doped carbon nanorods enabling electro-degradation of bulk organics

Jasper Biemolt [a], Koen van der Veen [a], Norbert J. Geels [a], Gadi Rothenberg [a], Ning Yan [a, b, *]

[a] Van 't Hoff Institute for Molecular Sciences, University of Amsterdam, Science Park 904, 1098XH, Amsterdam, the Netherlands
[b] School of Physics and Technology, Wuhan University, 430072, Wuhan, China

ARTICLE INFO

Article history:
Received 28 July 2019
Received in revised form
9 September 2019
Accepted 10 September 2019
Available online 10 September 2019

Keywords:
Electrocatalysis
Hydrogen peroxide synthesis
Oxygen reduction
Mesoporous carbon
Wastewater treatment

ABSTRACT

The direct synthesis of hydrogen peroxide using sustainable energy and molecular oxygen is a promising alternative approach to the conventional batch synthesis. Here we present a manganese and nitrogen co-doped carbon material which catalyzes the selective reduction of dioxygen in an acidic environment to hydrogen peroxide. The onset potential is close to 0.7 V, with >98% H_2O_2 selectivity in the range of 0.7 −0.5 V *vs* RHE. This is the highest reported to date, outperforming many bimetallic noble metal catalysts. Besides, this doped carbon material is hierarchically porous, featuring both a large mesopore volume (4.54 mL g^{-1}) *and* a high specific surface area (1333 m^2 g^{-1}). This enables the effective adsorption of bulky organics such as methylene blue (385 mg g^{-1}). Combined with the formation of hydroxyl radicals during electrochemical H_2O_2 generation, this material also enables the efficient electrochemical degradation of methylene blue, as evidenced by *in situ* UV−vis spectrometry.

1. Introduction

Industrial wastewater often contains toxic organic pollutants. Traditional water treatment traps these contaminants in the sludge, incurring a large environmental footprint [1–4]. Recently, electrochemical methods using electrons as "clean reagents" have attracted much attention [5–10]. In particular, the oxygen reduction reaction (ORR) takes advantage of the readily-available oxygen dissolved in the water to produce hydrogen peroxide. This reaction is often associated with the formation of hydroxyl and peroxyl radicals at the electrode [11–13]. These radicals can break up even the most resistant organic compounds. Yet converting O_2 electrocatalytically into H_2O_2 is no easy task. The state-of-the-art platinum catalysts often facilitate the 4-electron transfer reaction, producing mainly water with little H_2O_2 [14–16]. Alloying Pt with suitable transition metals such as Au and Hg can catalyze the 2-electron transfer reduction and boost the H_2O_2 selectivity to > 90% [17], but these catalysts are expensive and their working potential at the benchmark 1 mA cm^{-2} is often below 0.4 V vs RHE. As we and others recently showed carbon catalysts have excellent ORR activity in alkaline media [18–25]. But most of these are not H_2O_2-selective and show poor activity under acidic conditions [26]. There are exceptions: a carbon-based catalyst tailored to produce H_2O_2 selectively in an acidic electrolyte was reported by Liu et al. [27] Their material, made from MOF-5, showed a 0.42 V vs RHE onset potential and a H_2O_2 selectivity of 90%. Elsewhere, Fellinger et al. used acidic media for their mesoporous nitrogen-doped carbon, reporting an onset potential of 0.55 V vs RHE and 95% H_2O_2 selectivity (other high-performance H_2O_2 catalysts are listed in Table S1 in the supporting information).

Because the reactive hydroxyl radicals are short-lived, the organic contaminants must be adsorbed and held at the electrode in close proximity to the radical-generating sites. This means that the H_2O_2-formation catalyst should be a porous material, allowing the capture of the organic pollutants. Pollutants come in all sizes, and the pore structure of the electrode must be designed appropriately. For instance, simple aromatics such as benzene, toluene and xylene have kinetic diameters < 8 Å, fitting easily in micropores. But many dyes [28–31], surfactants [32,33] and pharmaceutical compounds [34,35] can be > 2 nm in size, requiring larger pores for effective adsorption and mass transfer. Ideally, we want hierarchically porous electrodes with a high micropore volume *and*

* Corresponding author. Van 't Hoff Institute for Molecular Sciences, University of Amsterdam, Science Park 904, 1098XH, Amsterdam, the Netherlands.
E-mail address: n.yan@uva.nl (N. Yan).

https://doi.org/10.1016/j.carbon.2019.09.034
0008-6223/

a high mesopore volume. Carbon materials are suitable electrode materials, due to their high conductivity, low cost and tunable pore structure. Many groups are working on this topic (see also Table S2 in the supporting information for details): Schuster et al. prepared a spherical mesoporous carbon with 2.32 $cm^3 g^{-1}$ pore volume and SSA of 2445 $m^2 g^{-1}$ via a complex double 'hard' templating method [36]. Elsewhere, Xu et al. reported the synthesis of hollow N–C nanospheres with a surface area of 3022 $m^2 g^{-1}$ and pore volume of 2.43 $cm^3 g^{-1}$ N–C using a 'soft' templating technique [37]. Using MOF-5 as the precursor, a hierarchically mesoporous carbon with a SSA of 2734 $m^2 g^{-1}$ and pore volume of 5.53 $cm^3 g^{-1}$ was reported by Srinivas et al. [32] We also reported a series of N–Cs with hierarchical porosity showing excellent catalytic activities using the same approach [18]. Yet making hierarchically porous carbons with a high surface area and a large mesopore volume remains a challenge [38,39].

Based on our recent research into nitrogen-doped carbon (N–C) catalysts, we hypothesized that an active and selective catalyst for reducing O_2 to H_2O_2 with a high pore volume would both capture bulky organic pollutants from water and catalyze their degradation. Here we report a facile synthesis of hierarchically Mn and N co-doped carbon nanorods (Mn–N–C) starting from nitrilotriacetic acid. This material, with its large pore volume of 4.54 $cm^3 g^{-1}$ and a high specific surface area of 1333 $m^2 g^{-1}$, can adsorb 385 mg g^{-1} of methylene blue (MB, a dye with many industrial applications) [33–37]. Importantly, our catalyst converts O_2 selectively into H_2O_2, exhibiting a high onset potential of *ca.* 0.7 V vs RHE in 0.1 M $HClO_4$. The hydroxyl radicals degrade the adsorbed MB in the adjacent area within the porous electrode (see schematic in Fig. 1). This combined adsorption and electrocatalytic activity opens new opportunities for wastewater treatment as well as for electrocatalysis applications.

2. Results and discussion

2.1. Synthesis and physical properties of Mn–N–C nanorods

The Mn–N–C nanorods were prepared by adapting our previously published method (detailed experimental procedures are included in the supporting information) [21]. Briefly, nanorods of the manganese nitrilotriacetate precursor were synthesized hydrothermally. Subsequent pyrolysis and acid-washing removed the MnO particles, yielding the Mn and N co-doped carbon (see Fig. 2a). Scanning transmission electron microscopy (STEM) measurements confirmed that all of the MnO particles were removed (Fig. 2b). The nanorods have abundant mesopores (D < 20 nm) which are visible in the magnified SEM image in Fig. 2c. These mesopores vary in size, enabling the adsorption of different contaminants. By comparing the high-resolution transmission electron microscopy (HRTEM) images in Fig. 2e and f, we confirmed that these mesopores were templated by the MnO nanoparticles. The pore walls are made of graphitic carbon shells. They are typically less than 20 layers in thickness, containing many worm-like micropores. This connectivity creates a hierarchical pore structure (*vide infra*).

Fig. 3a compares the powder XRD patterns of MnO/Mn–N–C and the Mn–N–C nanorods. Three strong peaks in MnO/Mn–N–C at $2\theta = 35.0°$, 40.7° and 58.8° correspond to the (111), (200) and (220) planes of MnO, respectively. The Mn–N–C nanorods had no residual MnO. The broad peak at $2\theta = 25°$ was assigned to the graphite (002) plane. From the Raman spectrum in Fig. 3b we infer that the Mn–N–C nanorods contain both ordered and disordered carbon domains, (*cf.* the D- and G-band at 1351 and 1588 cm^{-1}, respectively) [40]. Again, no MnO signal (typically below 800 cm^{-1}) was observed. The presence of Mn and N moieties in the carbon was verified by X-ray photoelectron spectroscopy (XPS, Fig. 3c). It revealed a 1.5% nitrogen content including graphitic, pyridinic and oxidized N, of which *ca.* 20% was pyridinic nitrogen [21].

We then studied the pore structure using both nitrogen adsorption and mercury intrusion porosimetry. The nitrogen adsorption isotherm (Fig. 4a), shows a combination of a H3 and H4 hysteresis loops, implying the presence of micro-, meso- and macropores [41]. A BET analysis gave a high specific surface area of 1333 $m^2 g^{-1}$. We used the Saito and Foley model to examine the micropore volume and micropore size distribution (see Fig. 4b). This model indicated a micropore volume of 0.76 mL g^{-1}, with most pores > 0.6 nm. As CO_2 is produced during the pyrolysis, these pores might be created by the typical CO_2 activation process [42]. For comparison, we measured under the same conditions a control sample of commercial activated carbon. This had a similar specific surface area of 1301 $m^2 g^{-1}$ and a micropore volume of 0.64 mL g^{-1}.

In the middle region of the isotherm, our Mn–N–C differs from the commercial carbon sample. The adsorption-desorption hysteresis of Mn–N–C nanorod suggests the existence of mesopores. Analysis of the isotherm using Gurvich model revealed a pore volume of 4.54 mLg^{-1} at 0.99 p/p^0 [43]. This value surpasses most of the porous carbon materials reported to date (for a detailed comparison see Table S2 in the supporting information). Most of the mesopores in our material are < 10 nm in diameter (see Fig. 4c). This well matches the observations from the TEM micrographs. The mesopore volume calculated from the mercury intrusion porosimetry (Fig. 4d) reached 3.45 mL g^{-1}, derived from the intruded volume between pore sizes 3.6–50 nm ($p = 29.6$ MPa for 50 nm, $\theta = 140°$, $\gamma = 0.48$ N m^{-1}). This is slightly lower than that obtained from N_2 adsorption. Most likely, the difference is caused by ink-bottle shaped pores where the pore opening is too small for mercury to enter. The pore size distribution shows that most of the

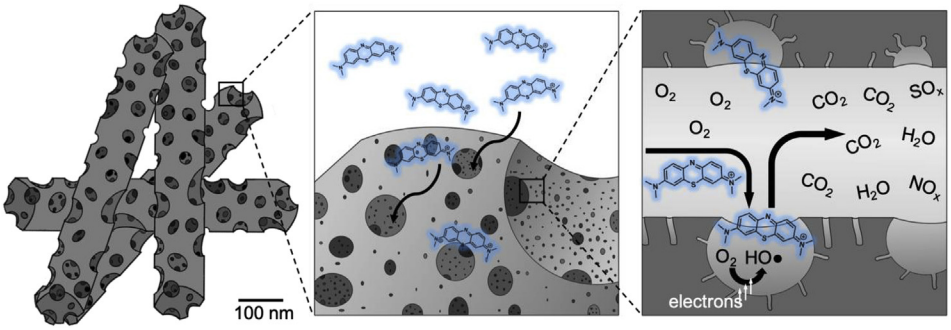

Fig. 1. The manganese and nitrogen co-doped carbon nanorods have macropores, mesopores and micropores, enabling the adsorption of large contaminant molecules such as methylene blue and their subsequent decomposition through the generation of hydroxyl radicals via simultaneous electrochemical oxygen reduction. (A colour version of this figure can be viewed online.)

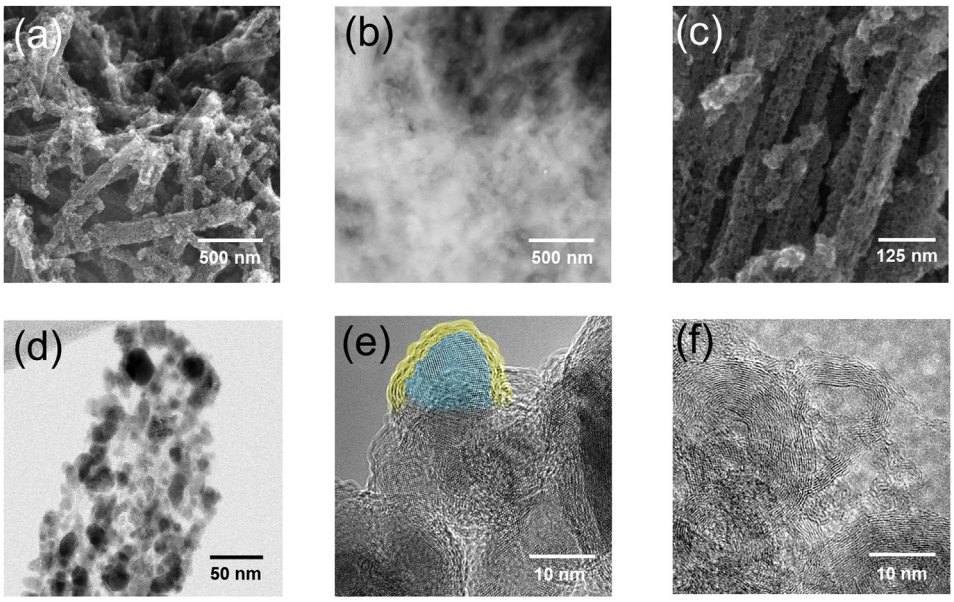

Fig. 2. (a) SEM and the corresponding (b) STEM images of the Mn–N–C nanorods; (c) magnified SEM image of Mn–N–C shows abundant mesopores in the nanorods; (d) bright-field TEM micrograph of a MnO-imbedded Mn–N–C nanorod; HRTEM micrographs of (e) the imbedded MnO template in Mn–N–C (colored in cyan and yellow respectively, unaltered version in Figure S2), and (f) the mesopores with graphitic shells of Mn–N–C after acid washing. (A colour version of this figure can be viewed online.)

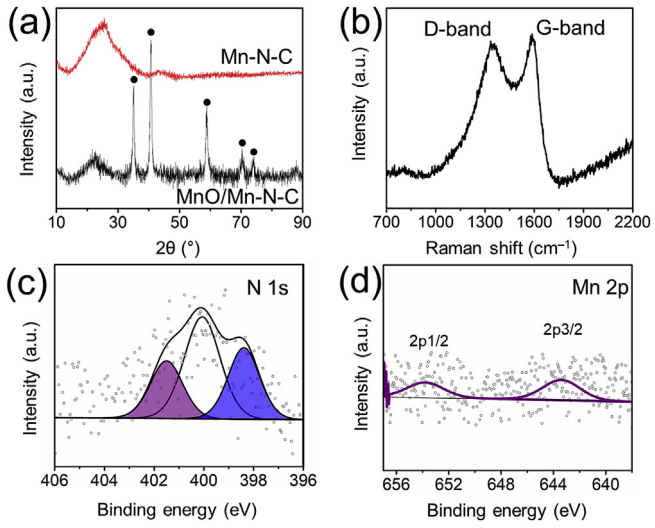

Fig. 3. (a) XRD of the MnO/Mn–N–C hybrid material and the Mn–N–C nanorods acquired after the acid wash with '●' symbols denoting the peaks for MnO, (b) the Raman spectrum and (c,d) the XP spectra of the Mn–N–C nanorods. (A colour version of this figure can be viewed online.)

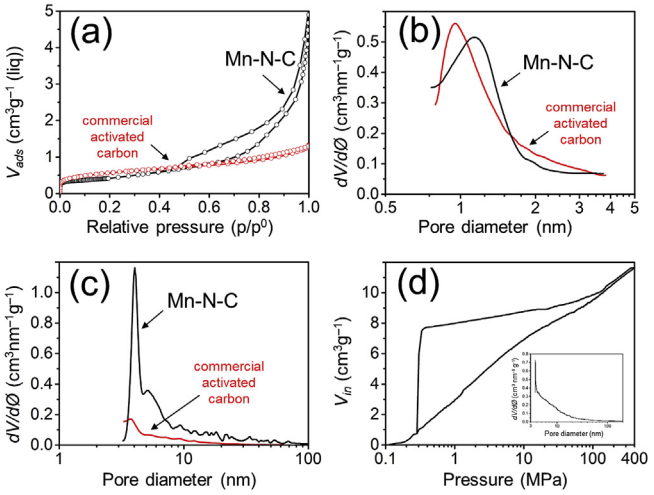

Fig. 4. (a) The N_2 adsorption isotherms at 77 K, adjusted to adsorbed liquid volume, (b) the micropore size distributions derived from the N_2 isotherms using the Saito and Foley analysis, (c) the mesopore size distributions from the N_2 isotherms using the Barrett-Joyner-Halenda analysis of the Mn–N–C nanorods and commercial activated carbon; and (d) the mercury intrusion curve of the Mn–N–C nanorods. (A colour version of this figure can be viewed online.)

pores are < 15 nm in diameter (inset of Fig. 4d, a high-resolution image is shown in Fig. S3).

2.2. Methylene blue adsorption

To evaluate the performance of our porous nanorods in the adsorption and electrocatalytic degradation of methylene blue (MB) illustrated in Fig. 1, we initially studied their capability of removing 50 ppm MB from an aqueous solution. This was compared to a commercial activated carbon which is essentially microporous with similar surface area (see Fig. 4a, b, 4c and Table 1 for the N_2 adsorption comparisons). After adding 5 mg of either Mn–N–C or activated carbon to 25 mL 50 ppm MB solution (pH was adjusted to 4 using HCl) and shaking gently, the blue color in the Mn–N–C suspension disappeared almost instantly. The complete removal of MB was confirmed by UV–visible spectroscopy (Fig. 5b). In contrast, the activated carbon suspension still displayed a light blue color even after 12 h agitation (see Fig. 5a). This implies that the carbon was already saturated by MB and could not remove the residual MB from the suspension.

To quantify the MB uptake, we measured its adsorption from solutions with varied concentrations, from 25 ppm up to 300 ppm. In each case, the amounts of adsorbed MB on the material and remaining MB in solution at equilibrium were measured and denoted as q_e (mg g^{-1}) and C_e, (mg L^{-1}), respectively. Fitting the q_e-C_e plot using established adsorption models can reveal the adsorption mechanism and maximum uptake of MB for each

Table 1
BET SSA, Saito and Foley micropore, BJH mesopore and BJH total pore volume of both the N–C and the commercial activated carbon.

Carbon	SSA (m^2g^{-1})	Micropore volume (mLg^{-1})	Gurvich pore volume[a] (mLg^{-1})	Hg intrusion mesopore volume (mLg^{-1})
N–C nanorods	1333	0.76	4.54	3.45
Commercial activated carbon (Norit Darco)	1301	0.64	0.75	n.a.

[a] Gurvich volume calculated with $p/p^0 = 0.99$.

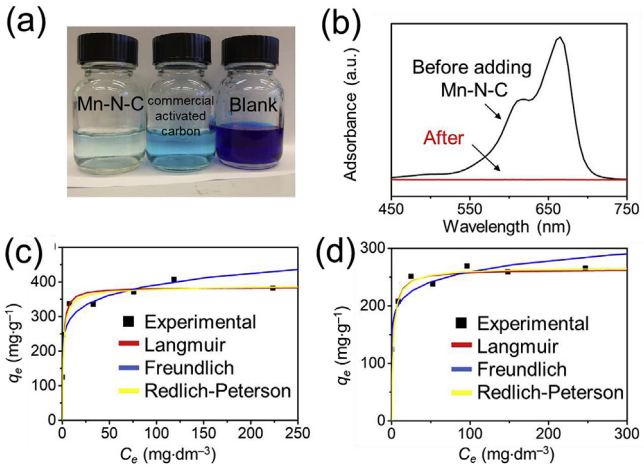

Fig. 5. (a) Photo of three vials containing 25 mL of a 50 ppm MB solutions after the addition of 5 mg Mn–N–C nanorods, 5 mg commercial activated carbon and nothing; (b) The UV–Vis spectrum of a 50 ppm MB solution before and after adding 5 mg Mn–N–C nanorods; Experimental data and fittings of the adsorption isotherm of MB for (c) Mn–N–C nanorods and (d) the commercial activated carbon. (A colour version of this figure can be viewed online.)

adsorbent [44]. Here we used the Langmuir, Freundlich and Redlich-Peterson adsorption models (see Supporting Information for details) [45–48]. The adsorption model parameters acquired from the linear fit of the models are summarized in Table S2. Fig. 5c and d compares the MB adsorption isotherms of the Mn–N–C nanorods and the commercial activated carbon. The commercial activated carbon clearly follows the Langmuir and Redlich-Peterson isotherm models, suggesting a monolayer adsorption of MB. The Mn–N–C results fit both the Langmuir and Freundlich model well, but show a maximum in the MB adsorption. When the Langmuir model is considered, we used the monolayer saturation capacity (Q), equaling to k_L/a_L, to quantify the maximum MB uptake in the adsorbent. Albeit that both samples showed a similar specific surface area, their Q values differ significantly: 385 mg g^{-1} for the Mn–N–C sample compared to only 263 mg g^{-1} for the commercial activated carbon.

In fact, when the molecular dimension of the adsorbate is sufficiently small, such as that of N_2, CO_2 and K^+/OH^-, the adsorption capability of the adsorbent can, in many cases, be simply maximized by increasing its specific surface area that is mainly attributed by the micropore. This principle has been applied in developing high-performance materials for supercapacitors and CO_2 adsorption [45-53]. However, when the molecular dimension of the adsorbate is large, such as that of dyes and surfactants, the adsorbate will transfer slowly in the adsorbent and can easily block the small micropores during the adsorption process (see the schematic comparison in Fig. S4). In this case, the material with more mesopores is much advantageous in capturing and accommodating these bulky molecules [31,54,55]. The large MB molecules (1.3–1.8 nm diameter [29,56,57]) may block the micropores of the commercial activated carbon [31,54,55]. In addition, the commercial activated carbon would also suffer from a lower mass transport. Consequently, our hierarchically porous Mn–N–C nanorods with high specific surface area and mesopore volume showed a superior capability in adsorbing MB.

2.3. Electrochemical production of H_2O_2

We studied the catalytic activity of Mn–N–C nanorods in producing H_2O_2 from the dissolved O_2 through the electrocatalytic oxygen reduction reaction. The ORR activity and selectivity of both the Mn–N–C nanorods and commercial activated carbon were tested in a 0.1 M $HClO_4$ electrolyte. Cyclic voltammetry using a rotating disc electrode in the N_2-saturated electrolyte only showed capacitive behaviors for both materials (Fig. S5). In the O_2-saturated electrolyte, reduction peaks at *ca.* 0.6 and 0.3 V vs RHE were observed for the Mn–N–C nanorods and commercial activated carbon, respectively, which confirmed that ORR has occurred at these potentials.

We then used a rotating ring disk electrode (RRDE) for evaluating the ORR activity and H_2O_2 selectivity. Fig. 6a compares the linear sweep voltammograms (LSVs) of the disk for three different samples: commercial activated carbon (red), Mn–N–C nanorods (black) and 20 wt% Pt/C (blue). The Mn–N–C nanorods have an onset potential of *ca.* 0.7 V vs RHE. This agrees with the observed potential from the ring when H_2O_2 oxidation starts (see Fig. 6b). This value is close to the standard reduction potential $E^0_{(O_2/H_2O_2)} = 0.7$ V and is among the highest reported for the O_2–H_2O_2 conversion [17,27,58–61]. Moreover, unlike many excellent carbon-based ORR catalysts [18,23,62,63], our Mn–N–C nanorods showed not only high activity in acidic media, but also exceptionally high H_2O_2 selectivity (98%) at potentials > 0.5 V vs RHE (see

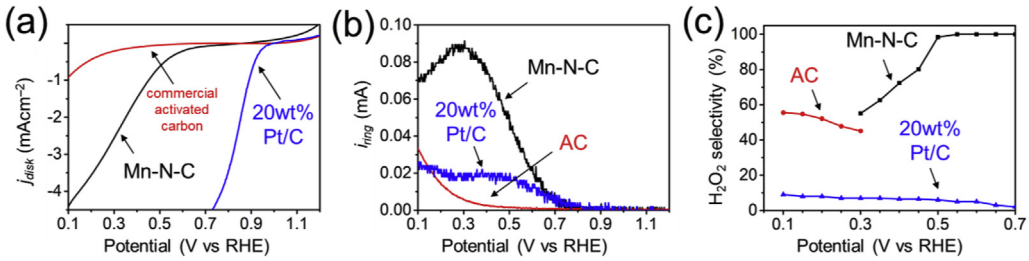

Fig. 6. (a) Disk current density and (b) ring current from the RRDE experiments; (c) the H_2O_2 selectivity at different potentials. The measurements were performed in a O_2 saturated 0.1 M $HClO_4$, with a scan rate of 10 mV s^{-1} and the rotating speed of 1600 rpm. (A colour version of this figure can be viewed online.)

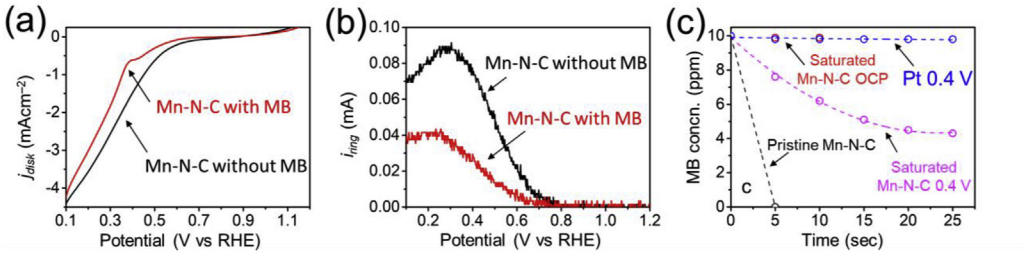

Fig. 7. (a) Disk current density and (b) ring current from the RRDE experiments in a O_2 saturated 0.1 M $HClO_4$ with and without the addition of 25 ppm MB, the scan rate is 10 mV s^{-1} and the rotating speed is 1600 rpm, (c) *in situ* UV–Vis measurements for the oxidation of MB by the N–C nanorods. (A colour version of this figure can be viewed online.)

Fig. 6c), which implied that the number of electron transferred was close to 2. At the benchmark 1 mA cm^{-2}, the potential reached 0.41 V vs RHE and the selectivity remained 74%, comparable with the noble metal catalyst. A detailed comparison with the state-of-the-art is included in Table S1. Note that the Pt/C showed better ORR activity with an onset potential of 0.92 V vs RHE, due to the 4-electron transfer reaction pathway in which the O_2 was fully reduced to H_2O. The H_2O_2 selectivity for the Pt/C catalyst was <10%, in good agreement with published results [64]. The commercial activated carbon is inactive in the acidic electrolyte, with a very low current and H_2O_2 yield. Besides, Mn–N–C also demonstrated excellent stability in terms of both O_2 activation and H_2O_2 selectivity in the 18 h longevity test (see Fig. S6).

2.4. Electrochemical degradation of methylene blue

H_2O_2 can hardly oxidize many "robust" organic pollutants directly (such as the aromatics and MB) [12,65]. Typically, the oxidation can only occurs via the scission of the peroxo bond and the generation of active free-radicals (eq (1)). Transition metal ions are often applied as the catalysts [66–68], as is the activated carbon [69,70]. Remarkably, the advantage of converting O_2 into H_2O_2 electrochemically is the formation *in situ* of these hydroxyl and peroxyl radical intermediates [11–13]. A 3-electron transfer process and a mono-electron reduction of H_2O_2 have been proposed as the two possible pathways (eqs (2) and (3)):

$$2H_2O_2 \rightarrow HOO^{\cdot} + HO^{\cdot} + H_2O \quad (1)$$

$$O_2 + 3H^+ + 3e^- \rightarrow HO^{\cdot} + H_2O \quad (2)$$

$$H_2O_2 + e^- + H^+ \rightarrow HO^{\cdot} + H_2O \quad (3)$$

With the presence of hydroxyl radicals, the complete oxidation of MB can be achieved following eq (4) with minimal toxic products release [71]. As the hydroxyl radicals can be rapidly reduced to hydroxyl ions, it is critical that MB is pre-adsorbed in the porous structure where the radical-generation sites are nearby (see Fig. 1).

$$C_{16}H_{18}N_3SCl \xrightarrow{51\ HO^{\cdot}} 16CO_2 + 6H_2O + H_2SO_4 + 3HNO_3 + HCl \quad (4)$$

Before studying the electrocatalytic degradation of MB, we first examined whether the adsorption of MB will cause the poison of our catalyst. Fig. 7a compares the performances of Mn–N–C nanorods with and without the presence of 25 ppm MB. Despite the fact that the reduction current has shifted a little to lower voltages due to the MB addition, the onset potential barely changed. This is also reflected by the unchanged onset potential, recorded at the ring in Fig. 7b, at which the production of H_2O_2 starts. The current drops in both the ring and disk after adding MB can be ascribed to (1) blockage of active site by adsorbed MB molecules and (2) the consumption of peroxyl or hydroxyl radicals by MB.

To study the electrocatalytic degradation of MB, we performed an *in-situ* UV–vis spectrometric study using a three-electrode cell. The electrolyte was also O_2-saturated 0.1 M $HClO_4$ containing 10 ppm MB and the working electrode was biased at 0.4 V vs RHE (see supporting information for details). Because the Pt wire reference electrode can catalyze the generation of hydroxyl radicals through eq. (1), we limited the test time to <30 s. We anticipated that this can avoid the contact between the generated H_2O_2 and Pt wire. In the Pt working electrode test, the concentration of MB remained constant in time (see Fig. 7c). Interestingly, the test with pristine Mn–N–C nanorod showed that all of the MB disappeared after only 5 s. However, this was not because of the electrocatalytic degradation of MB, but was ascribed to the rapid adsorption of MB on the working electrode. To exclude this artefact, we first immersed the Mn–N–C nanorod working electrode in 10 ppm electrolyte with sufficient volume. Then the MB-saturated working electrode, denoted as treated Mn–N–C, was then mounted in the *in situ* cell. A clear MB concentration decrease was observed progressively only when the potential was applied, confirming the electrocatalytic decomposition.

3. Conclusions

The decomposition of organic pollutants in water can be done efficiently if one combines adsorption, electrocatalysis, and free-radical reactions. Hierarchically porous carbon nanorods co-doped with manganese and nitrogen are ideal for this purpose, as they have both a large surface area and a high pore volume, as well as good active sites. These materials can adsorb large amounts of methylene blue from water (385 mg g^{-1}, 46% higher compared to a commercial activated carbon with a similar surface area). Importantly, they also catalyze the electrochemical reduction of dioxygen to hydrogen peroxide with >98% selectivity. *In situ* generation of hydroxyl free-radicals at the catalyst surface enables the efficient decomposition of methylene blue. The catalysts are made from abundant elements, and can be produced on gram scale. We hope that the results reported here will stimulate researchers to use these materials in a variety of applications.

Acknowledgement

We thank the financial support from the Netherlands Organisation for Scientific Research NWO-GDST Advanced Materials program (project No. 729.001.022), and the research fund through Wuhan University for the *in-situ* UV–vis measurement. This work is part of the Research Priority Area Sustainable Chemistry of the UvA (www.suschem.uva.nl).

Appendix A. Supplementary data

Supplementary data to this article can be found online at

https://doi.org/10.1016/j.carbon.2019.09.034.

References

[1] Y. Yang, Y. Zhao, A. Babatunde, L. Wang, Y. Ren, Y. Han, Characteristics and mechanisms of phosphate adsorption on dewatered alum sludge, Separ. Purif. Technol. 51 (2006) 193–200, https://doi.org/10.1016/j.seppur.2006.01.013.

[2] K.C. Makris, D. Sarkar, R. Datta, Aluminum-based drinking-water treatment residuals: a novel sorbent for perchlorate removal, Environ. Pollut. 140 (2006) 9–12, https://doi.org/10.1016/j.envpol.2005.08.075.

[3] A.O. Babatunde, Y.Q. Zhao, Constructive approaches toward water treatment works sludge management: an international review of beneficial reuses, Crit. Rev. Environ. Sci. Technol. 37 (2007) 129–164, https://doi.org/10.1080/10643380600776239.

[4] E. Igos, A. Dalle, L. Tiruta-Barna, E. Benetto, I. Baudin, Y. Mery, Life Cycle Assessment of water treatment: what is the contribution of infrastructure and operation at unit process level? J. Clean. Prod. 65 (2014) 424–431, https://doi.org/10.1016/j.jclepro.2013.07.061.

[5] E. Brillas, J.C. Calpe, J. Casado, Mineralization of 2,4-D by advanced electrochemical oxidation processes, Water Res. 34 (2000) 2253–2262, https://doi.org/10.1016/S0043-1354(99)00396-6.

[6] T.-C. An, X.-H. Zhu, Y. Xiong, Feasibility study of photoelectrochemical degradation of methylene blue with three-dimensional electrode-photocatalytic reactor, Chemosphere 46 (2002) 897–903, https://doi.org/10.1016/S0045-6535(01)00157-6.

[7] S. Yuan, M. Tian, Y. Cui, L. Lin, X. Lu, Treatment of nitrophenols by cathode reduction and electro-Fenton methods, J. Hazard Mater. 137 (2006) 573–580, https://doi.org/10.1016/j.jhazmat.2006.02.069.

[8] H. Ma, Q. Zhuo, B. Wang, Electro-catalytic degradation of methylene blue wastewater assisted by Fe2O3-modified kaolin, Chem. Eng. J. 155 (2009) 248–253, https://doi.org/10.1016/j.cej.2009.07.049.

[9] M.A. Hassan, M.M. El Jamal, Kinetic study of the electrochemical oxidation of methylene blue with Pt electrode, Port. Electrochim. Acta 30 (2012) 351–359, https://doi.org/10.4152/pea.201205351.

[10] L. Ma, M. Zhou, G. Ren, W. Yang, L. Liang, A highly energy-efficient flow-through electro-Fenton process for organic pollutants degradation, Electrochim. Acta 200 (2016) 222–230, https://doi.org/10.1016/j.electacta.2016.03.181.

[11] Q. Yue, K. Zhang, X. Chen, L. Wang, J. Zhao, J. Liu, J. Jia, Generation of OH radicals in oxygen reduction reaction at Pt–Co nanoparticles supported on graphene in alkaline solutions, Chem. Commun. 46 (2010) 3369, https://doi.org/10.1039/c000084a.

[12] J.-M. Noël, A. Latus, C. Lagrost, E. Volanschi, P. Hapiot, Evidence for OH radical production during electrocatalysis of oxygen reduction on Pt surfaces: consequences and application, J. Am. Chem. Soc. 134 (2012) 2835–2841, https://doi.org/10.1021/ja211663t.

[13] K. Sobańska, P. Pietrzyk, Z. Sojka, Generation of reactive oxygen species via electroprotic interaction of H_2O_2 with ZrO_2 gel: ionic sponge effect and pH-switchable peroxidase- and catalase-like activity, ACS Catal. 7 (2017) 2935–2947, https://doi.org/10.1021/acscatal.7b00189.

[14] Z. Wen, J. Liu, J. Li, Core/shell Pt/C nanoparticles embedded in mesoporous carbon as a methanol-tolerant cathode catalyst in direct methanol fuel cells, Adv. Mater. 20 (2008) 743–747, https://doi.org/10.1002/adma.200701578.

[15] M. Inaba, M. Ando, A. Hatanaka, A. Nomoto, K. Matsuzawa, A. Tasaka, T. Kinumoto, Y. Iriyama, Z. Ogumi, Controlled growth and shape formation of platinum nanoparticles and their electrochemical properties, Electrochim. Acta 52 (2006) 1632–1638, https://doi.org/10.1016/j.electacta.2006.03.094.

[16] R. Kou, Y. Shao, D. Wang, M.H. Engelhard, J.H. Kwak, J. Wang, V.V. Viswanathan, C. Wang, Y. Lin, Y. Wang, I.A. Aksay, J. Liu, Enhanced activity and stability of Pt catalysts on functionalized graphene sheets for electrocatalytic oxygen reduction, Electrochem. Commun. 11 (2009) 954–957, https://doi.org/10.1016/j.elecom.2009.02.033.

[17] S. Siahrostami, A. Verdaguer-Casadevall, M. Karamad, D. Deiana, P. Malacrida, B. Wickman, M. Escudero-Escribano, E.A. Paoli, R. Frydendal, T.W. Hansen, I. Chorkendorff, I.E.L. Stephens, J. Rossmeisl, Enabling direct H2O2 production through rational electrocatalyst design, Nat. Mater. 12 (2013) 1137–1143, https://doi.org/10.1038/nmat3795.

[18] D. Eisenberg, W. Stroek, N.J. Geels, C.S. Sandu, A. Heller, N. Yan, G. Rothenberg, A simple synthesis of an N-doped carbon ORR catalyst: hierarchical micro/meso/macro porosity and graphitic shells, Chem. Eur J. 22 (2016) 501–505, https://doi.org/10.1002/chem.201504568.

[19] D. Eisenberg, W. Stroek, N.J. Geels, S. Tanase, M. Ferbinteanu, S.J. Teat, P. Mettraux, N. Yan, G. Rothenberg, A rational synthesis of hierarchically porous, N-doped carbon from Mg-based MOFs: understanding the link between nitrogen content and oxygen reduction electrocatalysis, Phys. Chem. Chem. Phys. 18 (2016) 20778–20783, https://doi.org/10.1039/C6CP04132A.

[20] D. Eisenberg, P. Prinsen, N.J. Geels, W. Stroek, N. Yan, B. Hua, J.-L. Luo, G. Rothenberg, The evolution of hierarchical porosity in self-templated nitrogen-doped carbons and its effect on oxygen reduction electrocatalysis, RSC Adv. 6 (2016) 80398–80407, https://doi.org/10.1039/C6RA16606G.

[21] J. Pandey, B. Hua, W. Ng, Y. Yang, K. van der Veen, J. Chen, N.J. Geels, J.-L. Luo, G. Rothenberg, N. Yan, Developing hierarchically porous MnOx/NC hybrid nanorods for oxygen reduction and evolution catalysis, Green Chem. 19 (2017) 2793–2797, https://doi.org/10.1039/C7GC00147A.

[22] K. Gong, F. Du, Z. Xia, M. Durstock, L. Dai, Nitrogen-doped carbon nanotube Arrays with high electrocatalytic activity for oxygen reduction, Science 323 (2009) 760–764, https://doi.org/10.1126/science.1168049.

[23] L. Yang, S. Jiang, Y. Zhao, L. Zhu, S. Chen, X. Wang, Q. Wu, J. Ma, Y. Ma, Z. Hu, Boron-doped carbon nanotubes as metal-free electrocatalysts for the oxygen reduction reaction, Angew. Chem. 123 (2011) 7270–7273, https://doi.org/10.1002/ange.201101287.

[24] W. Wei, H. Liang, K. Parvez, X. Zhuang, X. Feng, K. Müllen, Nitrogen-doped carbon nanosheets with size-defined mesopores as highly efficient metal-free catalyst for the oxygen reduction reaction, Angew. Chem. 126 (2014) 1596–1600, https://doi.org/10.1002/ange.201307319.

[25] X. He, S.Z. Luan, L. Wang, R.Y. Wang, P. Du, Y.Y. Xu, H.J. Yang, Y.G. Wang, K. Huang, M. Lei, Facile loading mesoporous Co3O4 on nitrogen doped carbon matrix as an enhanced oxygen electrode catalyst, Mater. Lett. 244 (2019) 78–82, https://doi.org/10.1016/j.matlet.2019.01.144.

[26] Y. Jiang, P. Ni, C. Chen, Y. Lu, P. Yang, B. Kong, A. Fisher, X. Wang, Selective electrochemical H_2O_2 production through two-electron oxygen electrochemistry, Adv. Energy Mater. 8 (2018) 1801909, https://doi.org/10.1002/aenm.201801909.

[27] Y. Liu, X. Quan, X. Fan, H. Wang, S. Chen, High-yield electrosynthesis of hydrogen peroxide from oxygen reduction by hierarchically porous carbon, Angew. Chem. 127 (2015) 6941–6945, https://doi.org/10.1002/ange.201502396.

[28] H. Tamai, T. Kakii, Y. Hirota, T. Kumamoto, H. Yasuda, Synthesis of extremely large mesoporous activated carbon and its unique adsorption for giant molecules, Chem. Mater. 8 (1996) 454–462, https://doi.org/10.1021/cm950381t.

[29] J. de S. Macedo, N.B. da Costa Júnior, L.E. Almeida, E.F. da S. Vieira, A.R. Cestari, I. de F. Gimenez, N.L. Villarreal Carreño, L.S. Barreto, Kinetic and calorimetric study of the adsorption of dyes on mesoporous activated carbon prepared from coconut coir dust, J. Colloid Interface Sci. 298 (2006) 515–522, https://doi.org/10.1016/j.jcis.2006.01.021.

[30] D.D. Asouhidou, K.S. Triantafyllidis, N.K. Lazaridis, K.A. Matis, S.-S. Kim, T.J. Pinnavaia, Sorption of reactive dyes from aqueous solutions by ordered hexagonal and disordered mesoporous carbons, Microporous Mesoporous Mater. 117 (2009) 257–267, https://doi.org/10.1016/j.micromeso.2008.06.034.

[31] X. Zhuang, Y. Wan, C. Feng, Y. Shen, D. Zhao, Highly efficient adsorption of bulky dye molecules in wastewater on ordered mesoporous carbons, Chem. Mater. 21 (2009) 706–716, https://doi.org/10.1021/cm8028577.

[32] A.S. Sirotkin, L.Yu Koshkina, K.G. Ippolitov, The BAC-process for treatment of waste water Containing non-ionogenic synthetic surfactants, Water Res. 35 (2001) 3265–3271, https://doi.org/10.1016/S0043-1354(01)00029-X.

[33] F. Karray, M. Mezghani, N. Mhiri, B. Djelassi, S. Sayadi, Scale-down studies of membrane bioreactor degrading anionic surfactants wastewater: isolation of new anionic-surfactant degrading bacteria, Int. Biodeterior. Biodegrad. 114 (2016) 14–23, https://doi.org/10.1016/j.ibiod.2016.05.020.

[34] E.K. Putra, R. Pranowo, J. Sunarso, N. Indraswati, S. Ismadji, Performance of activated carbon and bentonite for adsorption of amoxicillin from wastewater: mechanisms, isotherms and kinetics, Water Res. 43 (2009) 2419–2430, https://doi.org/10.1016/j.watres.2009.02.039.

[35] T.X. Bui, H. Choi, Adsorptive removal of selected pharmaceuticals by mesoporous silica SBA-15, J. Hazard Mater. 168 (2009) 602–608, https://doi.org/10.1016/j.jhazmat.2009.02.072.

[36] J. Schuster, G. He, B. Mandlmeier, T. Yim, K.T. Lee, T. Bein, L.F. Nazar, Spherical ordered mesoporous carbon nanoparticles with high porosity for lithium–sulfur batteries, Angew. Chem. Int. Ed. 51 (2012) 3591–3595, https://doi.org/10.1002/anie.201107817.

[37] F. Xu, Z. Tang, S. Huang, L. Chen, Y. Liang, W. Mai, H. Zhong, R. Fu, D. Wu, Facile synthesis of ultrahigh-surface-area hollow carbon nanospheres for enhanced adsorption and energy storage, Nat. Commun. 6 (2015) 7221, https://doi.org/10.1038/ncomms8221.

[38] G. Srinivas, V. Krungleviciute, Z.-X. Guo, T. Yildirim, Exceptional CO_2 capture in a hierarchically porous carbon with simultaneous high surface area and pore volume, Energy Environ. Sci. 7 (2014) 335–342, https://doi.org/10.1039/C3EE42918K.

[39] A.F. Strickland, W.S. Perkins, Decolorization of continuous dyeing wastewater by ozonation, Text. Chem. Color. 27 (1995) 11–15.

[40] A. Sadezky, H. Muckenhuber, H. Grothe, R. Niessner, U. Pöschl, Raman microspectroscopy of soot and related carbonaceous materials: spectral analysis and structural information, Carbon 43 (2005) 1731–1742, https://doi.org/10.1016/j.carbon.2005.02.018.

[41] M. Thommes, K. Kaneko, A.V. Neimark, J.P. Olivier, F. Rodriguez-Reinoso, J. Rouquerol, K.S.W. Sing, Physisorption of gases, with special reference to the evaluation of surface area and pore size distribution (IUPAC Technical Report), Pure Appl. Chem. 87 (2015), https://doi.org/10.1515/pac-2014-1117.

[42] F. Rodríguez-Reinoso, M. Molina-Sabio, M.T. González, The use of steam and CO2 as activating agents in the preparation of activated carbons, Carbon 33 (1995) 15–23, https://doi.org/10.1016/0008-6223(94)00100-E.

[43] L.G. Gurvich, Zhurnal Rus. Fiz.-Khimicheskago Obshchestva. (1915) 805–827.

[44] K.Y. Foo, B.H. Hameed, Insights into the modeling of adsorption isotherm systems, Chem. Eng. J. 156 (2010) 2–10, https://doi.org/10.1016/j.cej.2009.09.013.

[45] E.N. El Qada, S.J. Allen, G.M. Walker, Adsorption of Methylene Blue onto activated carbon produced from steam activated bituminous coal: a study of equilibrium adsorption isotherm, Chem. Eng. J. 124 (2006) 103–110, https://

doi.org/10.1016/j.cej.2006.08.015.
[46] A.M.M. Vargas, A.L. Cazetta, M.H. Kunita, T.L. Silva, V.C. Almeida, Adsorption of methylene blue on activated carbon produced from flamboyant pods (Delonix regia): study of adsorption isotherms and kinetic models, Chem. Eng. J. 168 (2011) 722–730, https://doi.org/10.1016/j.cej.2011.01.067.
[47] M.U. Dural, L. Cavas, S.K. Papageorgiou, F.K. Katsaros, Methylene blue adsorption on activated carbon prepared from Posidonia oceanica (L.) dead leaves: kinetics and equilibrium studies, Chem. Eng. J. 168 (2011) 77–85, https://doi.org/10.1016/j.cej.2010.12.038.
[48] K. Mahmoudi, N. Hamdi, E. Srasra, Study of adsorption of methylene blue onto activated carbon from lignite, Surf. Eng. Appl. Electrochem. 51 (2015) 427–433, https://doi.org/10.3103/S1068375515050105.
[49] A. Wahby, J.M. Ramos-Fernández, M. Martínez-Escandell, A. Sepúlveda-Escribano, J. Silvestre-Albero, F. Rodríguez-Reinoso, High-surface-area carbon molecular sieves for selective CO2 adsorption, ChemSusChem 3 (2010) 974–981, https://doi.org/10.1002/cssc.201000083.
[50] Z. Yang, Y. Xia, R. Mokaya, Enhanced hydrogen storage capacity of high surface area zeolite-like carbon materials, J. Am. Chem. Soc. 129 (2007) 1673–1679, https://doi.org/10.1021/ja067149g.
[51] Y. Zhu, S. Murali, M.D. Stoller, K.J. Ganesh, W. Cai, P.J. Ferreira, A. Pirkle, R.M. Wallace, K.A. Cychosz, M. Thommes, D. Su, E.A. Stach, R.S. Ruoff, Carbon-based supercapacitors produced by activation of graphene, Science 332 (2011) 1537–1541, https://doi.org/10.1126/science.1200770.
[52] W. Chaikittisilp, K. Ariga, Y. Yamauchi, A new family of carbon materials: synthesis of MOF-derived nanoporous carbons and their promising applications, J. Mater. Chem. 1 (2013) 14–19, https://doi.org/10.1039/C2TA00278G.
[53] Y.S. Yun, S.Y. Cho, J. Shim, B.H. Kim, S.-J. Chang, S.J. Baek, Y.S. Huh, Y. Tak, Y.W. Park, S. Park, H.-J. Jin, Microporous carbon nanoplates from regenerated silk proteins for supercapacitors, Adv. Mater. 25 (2013) 1993–1998, https://doi.org/10.1002/adma.201204692.
[54] C. Pelekani, V.L. Snoeyink, A kinetic and equilibrium study of competitive adsorption between atrazine and Congo red dye on activated carbon: the importance of pore size distribution, Carbon 39 (2001) 25–37, https://doi.org/10.1016/S0008-6223(00)00078-6.
[55] Q. Li, V.L. Snoeyink, B.J. Mariñas, C. Campos, Pore blockage effect of NOM on atrazine adsorption kinetics of PAC: the roles of PAC pore size distribution and NOM molecular weight, Water Res. 37 (2003) 4863–4872, https://doi.org/10.1016/j.watres.2003.08.018.
[56] M. Arias, E. López, A. Nuñez, D. Rubinos, B. Soto, M.T. Barral, F. Díaz-Fierros, Adsorption of methylene blue by red mud, an oxide- rich byproduct of bauxite refining, in: J. Berthelin, P.M. Huang, J.-M. Bollag, F. Andreux (Eds.), Eff. Miner.-Org.-Microorg. Interact. Soil Freshw. Environ, Springer US, Boston, MA, 1999, pp. 361–365, https://doi.org/10.1007/978-1-4615-4683-2_39.
[57] P. Simoncic, T. Armbruster, Cationic methylene blue incorporated into zeolite mordenite-Na: a single crystal X-ray study, Microporous Mesoporous Mater. 81 (2005) 87–95, https://doi.org/10.1016/j.micromeso.2005.01.019.
[58] Y. Sun, I. Sinev, W. Ju, A. Bergmann, S. Dresp, S. Kühl, C. Spöri, H. Schmies, H. Wang, D. Bernsmeier, B. Paul, R. Schmack, R. Kraehnert, B. Roldan Cuenya, P. Strasser, Efficient electrochemical hydrogen peroxide production from molecular oxygen on nitrogen-doped mesoporous carbon catalysts, ACS Catal. 8 (2018) 2844–2856, https://doi.org/10.1021/acscatal.7b03464.
[59] T.-P. Fellinger, F. Hasché, P. Strasser, M. Antonietti, Mesoporous nitrogen-doped carbon for the electrocatalytic synthesis of hydrogen peroxide, J. Am. Chem. Soc. 134 (2012) 4072–4075, https://doi.org/10.1021/ja300038p.
[60] F. Hasché, M. Oezaslan, P. Strasser, T.-P. Fellinger, Electrocatalytic hydrogen peroxide formation on mesoporous non-metal nitrogen-doped carbon catalyst, J. Energy Chem. 25 (2016) 251–257, https://doi.org/10.1016/j.jechem.2016.01.024.
[61] A. Verdaguer-Casadevall, D. Deiana, M. Karamad, S. Siahrostami, P. Malacrida, T.W. Hansen, J. Rossmeisl, I. Chorkendorff, I.E.L. Stephens, Trends in the electrochemical synthesis of H_2O_2: enhancing activity and selectivity by electrocatalytic site engineering, Nano Lett. 14 (2014) 1603–1608, https://doi.org/10.1021/nl500037x.
[62] W. Ding, Z. Wei, S. Chen, X. Qi, T. Yang, J. Hu, D. Wang, L.-J. Wan, S.F. Alvi, L. Li, Space-confinement-induced synthesis of pyridinic- and pyrrolic-nitrogen-doped graphene for the catalysis of oxygen reduction, Angew. Chem. 125 (2013) 11971–11975, https://doi.org/10.1002/ange.201303924.
[63] T. Najam, S.S.A. Shah, W. Ding, J. Jiang, L. Jia, W. Yao, L. Li, Z. Wei, An efficient anti-poisoning catalyst against SOx, NOx, and POx: P, N-doped carbon for oxygen reduction in acidic media, Angew. Chem. 130 (2018) 15321–15326, https://doi.org/10.1002/ange.201808383.
[64] H. Liu, J. Li, X. Xu, F. Wang, J. Liu, Z. Li, J. Ji, Highly graphitic carbon black-supported platinum nanoparticle catalyst and its enhanced electrocatalytic activity for the oxygen reduction reaction in acidic medium, Electrochim. Acta 93 (2013) 25–31, https://doi.org/10.1016/j.electacta.2013.01.090.
[65] B.H.J. Bielski, D.E. Cabelli, Superoxide and hydroxyl radical Chemistry in aqueous solution, in: C.S. Foote, J.S. Valentine, A. Greenberg, J.F. Liebman (Eds.), Act. Oxyg. Chem, Springer Netherlands, Dordrecht, 1995, pp. 66–104, https://doi.org/10.1007/978-94-007-0874-7_3.
[66] H.J.H. Fenton, LXXIII.—oxidation of tartaric acid in presence of iron, J. Chem. Soc. Trans. 65 (1894) 899–910, https://doi.org/10.1039/CT8946500899.
[67] A. Xu, X. Li, S. Ye, G. Yin, Q. Zeng, Catalyzed oxidative degradation of methylene blue by in situ generated cobalt (II)-bicarbonate complexes with hydrogen peroxide, Appl. Catal. B Environ. 102 (2011) 37–43, https://doi.org/10.1016/j.apcatb.2010.11.022.
[68] L. Cheng, M. Wei, L. Huang, F. Pan, D. Xia, X. Li, A. Xu, Efficient H_2O_2 oxidation of organic dyes catalyzed by simple copper(II) ions in bicarbonate aqueous solution, Ind. Eng. Chem. Res. 53 (2014) 3478–3485, https://doi.org/10.1021/ie403801f.
[69] G. Fang, C. Liu, J. Gao, D. Zhou, New insights into the mechanism of the catalytic decomposition of hydrogen peroxide by activated carbon: implications for degradation of diethyl phthalate, Ind. Eng. Chem. Res. 53 (2014) 19925–19933, https://doi.org/10.1021/ie504184r.
[70] A. Asghar, A.A. Abdul Raman, W.M.A. Wan Daud, Advanced oxidation processes for in-situ production of hydrogen peroxide/hydroxyl radical for textile wastewater treatment: a review, J. Clean. Prod. 87 (2015) 826–838, https://doi.org/10.1016/j.jclepro.2014.09.010.
[71] M. Panizza, A. Barbucci, R. Ricotti, G. Cerisola, Electrochemical degradation of methylene blue, Separ. Purif. Technol. 54 (2007) 382–387, https://doi.org/10.1016/j.seppur.2006.10.010.